Joule

CellPress

Article

Unraveling the Nanoscale Heterogeneity of Solid Electrolyte Interphase Using Tip-Enhanced Raman Spectroscopy

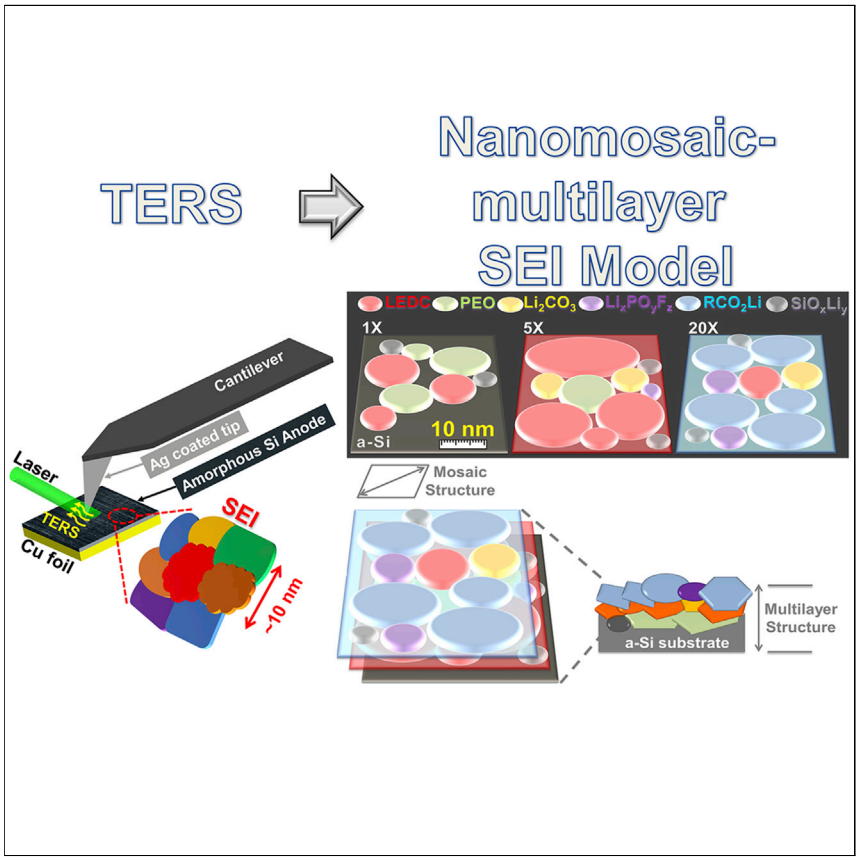

This article probes one of the key fundamental factors that determines the safety and life of Lithium-ion batteries known as "solid electrolyte interphase" (SEI). In this work, we provided a mechanistic picture on how the SEI evolves with battery cycling by investigating the SEI chemical composition and topography by using state-of-the-art tip-enhanced Raman spectroscopy (TERS).

Jagjit Nanda, Guang Yang, Tingzheng Hou, ..., Kristin Persson, Gabriel M. Veith, Alexei P. Sokolov

nandaj@ornl.gov (J.N.)
yangg@ornl.gov (G.Y.)

HIGHLIGHTS

TERS measures the topography and chemical heterogeneity of SEI on a-Si at nanoscale

SEI composition of SEI constantly evolves with progressive galvanostatic cycling

TERS can provide molecular level conformational changes

A nanomosaic-multilayer model for SEI on a-Si is proposed

Nanda et al., Joule 3, 1–19
August 21, 2019
https://doi.org/10.1016/j.joule.2019.05.026

Please cite this article in press as: Nanda et al., Unraveling the Nanoscale Heterogeneity of Solid Electrolyte Interphase Using Tip-Enhanced Raman Spectroscopy, Joule (2019), https://doi.org/10.1016/j.joule.2019.05.026

Joule

CellPress

Article

Unraveling the Nanoscale Heterogeneity of Solid Electrolyte Interphase Using Tip-Enhanced Raman Spectroscopy

Jagjit Nanda,[1,6,7,*] Guang Yang,[1,5,6,*] Tingzheng Hou,[2] Dmitry N. Voylov,[4] Xin Li,[1] Rose E. Ruther,[1] Michael Naguib,[3] Kristin Persson,[2] Gabriel M. Veith,[1] and Alexei P. Sokolov[1,4,5]

SUMMARY

We employ tip-enhanced Raman spectroscopy (TERS) to study model amorphous silicon (a-Si) thin film anodes galvanostatically cycled for different numbers. For the 1× cycled a-Si, TERS shows good correlation between solid electrolyte interphase (SEI) topography and chemical mapping, corresponding to distribution of lithium ethylene dicarbonate (LEDC) and poly (ethylene oxide) (PEO)-like oligomer species. Subsequent electrochemical cycling makes the SEI relatively thick and rough with the chemical composition heavily dominated by LEDC monomer-dimer for 5× cycled a-Si. For 20× cycled a-Si, the TERS signal is dominated by carboxylate (RCO_2Li) compounds of various conformations and fluorinated species ($Li_xPO_yF_z$). A nanomosaic-multilayer hybrid SEI model on top of the a-Si anode is proposed. The significance of this work is applicable not only to silicon, where SEI plays a dominant role in determining the cycle life performance and reversibility, but also for a number of other relevant battery chemistries such as Na-ion and multivalent redox systems.

INTRODUCTION

Passivated interfaces between the electrode and electrolyte are often the key to the performance, stability, and safety of electrochemical energy storage devices.[1–4] An important example is the solid electrolyte interphase (SEI), which primarily originates as a result of the reductive decomposition of electrolytes on the negative electrode (anode). A well-formed and chemically stable SEI protects degradation of the electrode and at the same time allows uninterrupted ion transport during charge-discharge.[5] On the contrary, uncontrolled and chemically reactive SEI growth significantly affects Coulombic efficiency, increases electrode polarization, and contributes to the loss of lithium inventory amounting to capacity and power fade.[6] Numerous studies have been carried out for more than two decades to understand the mechanism of SEI formation and quantify the composition, thickness, and ion transport.[7] Despite such progress, a unified picture encompassing the morphology, phase, and chemical composition of SEI is still lacking. To date, two SEI models are generally accepted on Li-ion battery anodes: the mosaic-type polyhetero microphase model proposed by Peled et al.[8] and the multilayer model proposed by Aurbach et al.[9] The former was experimentally supported by time-of-flight secondary-ion mass spectrometry (TOF-SIMS) measurements with micron-scale lateral special resolution.[10] The latter model was based on the time-resolved electrochemical impedance measurement. Extensive follow-up studies on surface chemistry of the SEI were implemented based on a variety of characterization techniques, such as Fourier-transform infrared spectroscopy (FTIR),[11] Raman spectroscopy,[12] X-ray photoelectron

Context & Scale

Solid electrolyte interphase (SEI) is considered the key component responsible for the safety, performance, and life for most secondary batteries. Despite this, a unified picture encompassing its chemical composition, distribution of phases, and topography at nanoscale is still lacking. We report the first observation of nanoscale chemical and topographical heterogeneity of a SEI formed on amorphous silicon (a-Si) using tip-enhanced Raman spectroscopy (TERS). Unlike ensemble averaged and relatively bulk sensitive vibrational spectroscopic techniques such as Raman and Fourier-transform infrared (FTIR), TERS is sensitive to dynamical evolution of the SEI at a lateral resolution of <10 nm and a sampling depth of <5 nm. The TERS results and analysis here can be broadly applicable for several other redox chemistries for Na-ion, solid-state, and metal air batteries. This study demonstrates that multi-modal spectroscopy like TERS can provide a useful mechanistic link between nanoscale morphology, interfacial transport, and the overall electrochemical performance.

spectroscopy (XPS),[13] nuclear magnetic resonance (NMR) spectroscopy,[14] neutron reflectometry (NR),[15] and small-angle neutron scattering (SANS).[16] Despite much effort, the comprehensive image of the SEI model is still elusive, especially in the nanoscale. This is due to the lack of an effective experimental means to depict the nanoscale spatial heterogeneity of the SEI and correlate the chemical information of the SEI species to its topography. This calls for the development of enabling multi-modal interfacial techniques that capture both chemical composition as well as the surface topography of SEI with nanoscale resolution. The complexity of SEI growth and its evolution is multiplied several fold for alloy anodes such as silicon, where there are (1) tremendous volume changes upon lithiation (delithation), and (2) complex surface chemical composition and heterogeneity. The severe volumetric change of the silicon anode results in the SEI layer constantly breaking and reforming with evolving chemical composition during electrochemical cycling and further leads to irreversible capacity fade and loss of lithium inventory. Recent literature studies report a highly heterogeneous and multiphasic SEI for silicon that constantly evolves during continuous electrochemical cycling.[7,17] In addition, almost all silicon surfaces have a native oxide or sub-oxide layer that reacts irreversibly during the initial electrochemical cycles.[12] This brings up an important question—what the local structure of the SEI is upon passivation of native silicon||silicon oxide surfaces.[18]

Tip-enhanced Raman spectroscopy (TERS) is a highly surface sensitive method based on the plasmonic response of a metallic tip. A confined surface plasmon enhances the local electric field and thereby increases the Raman cross section of the analyte molecule.[19–22] In ideal cases, TERS can detect single molecules and their conformational variations when the molecules are in a gap between the tip and a smooth metallic substrate (the so-called gap-mode TERS).[23,24] To date, a few TERS studies have been reported on metallic surface-bound molecules,[25,26] separated large biomolecules on atomically smooth substrates,[27] and low-dimensional nano objects.[28–30] Although it has been demonstrated to be capable of probing the sequence in a single RNA strand,[31] non-gap mode TERS is still extremely challenging to perform because of its much smaller enhancement factor (EF) than gap-mode TERS, especially for molecules with a small Raman scattering cross section.[32] In a practical electrochemical energy storage system, the galvanostatically cycled electrode surface becomes roughened upon cycling, and the surface molecular configuration is extremely complicated; TERS has thus never been effectively used for probing the surface chemistry on a battery electrode. Herein, using electrochemically cycled amorphous silicon (a-Si), we report the first TERS study to unveil the surface chemistry of the electrode at nanoscale. For the first time, the SEI topography and chemical composition at nanometer lateral resolution were correlated, and the SEI composition as a function of electrochemical cycling on a-Si was reported. The dominant SEI species for a-Si cycled galvanostatically vary with electrochemical cycling. We show that primary SEI species are the poly (ethylene oxide) (PEO)-like oligomer and lithium ethylene dicarbonate (LEDC) $(CH_2OCOOLi)_2$ for a-Si cycled once (denoted as 1× a-Si), mainly LEDC for 5× a-Si and carboxylate compounds for 20× a-Si. Further, assisted by density-functional theory (DFT), we demonstrate that TERS captures various conformational changes of carboxylate molecules upon coordination to lithium cations for the 20× a-Si. Such molecular level configuration of SEI species is not readily accomplished by any other characterization method. A statistical analysis on the TERS mapping using principal component analysis (PCA) and multivariate curve resolution (MCR) quantifies the abundance of the distribution of the characteristic spectra of related SEI species. Based on the TERS analysis, we unveil the nanoscale structure of the SEI on a-Si under extended galvanostatic cycles and propose a new nanomosaic-multilayer model for SEI, in which the

[1]Oak Ridge National Laboratory, Oak Ridge, TN 37831, USA

[2]Department of Materials Science and Engineering, University of California Berkeley, 210 Hearst Mining Building, Berkeley, CA 94704, USA

[3]Department of Physics and Engineering Physics, Tulane University, New Orleans, LA, 70118, USA

[4]Department of Chemistry, University of Tennessee, Knoxville, TN 37996, USA

[5]Senior author

[6]These authors contributed equally

[7]Lead Contact

*Correspondence: nandaj@ornl.gov (J.N.), yangg@ornl.gov (G.Y.)

https://doi.org/10.1016/j.joule.2019.05.026

Please cite this article in press as: Nanda et al., Unraveling the Nanoscale Heterogeneity of Solid Electrolyte Interphase Using Tip-Enhanced Raman Spectroscopy, Joule (2019), https://doi.org/10.1016/j.joule.2019.05.026

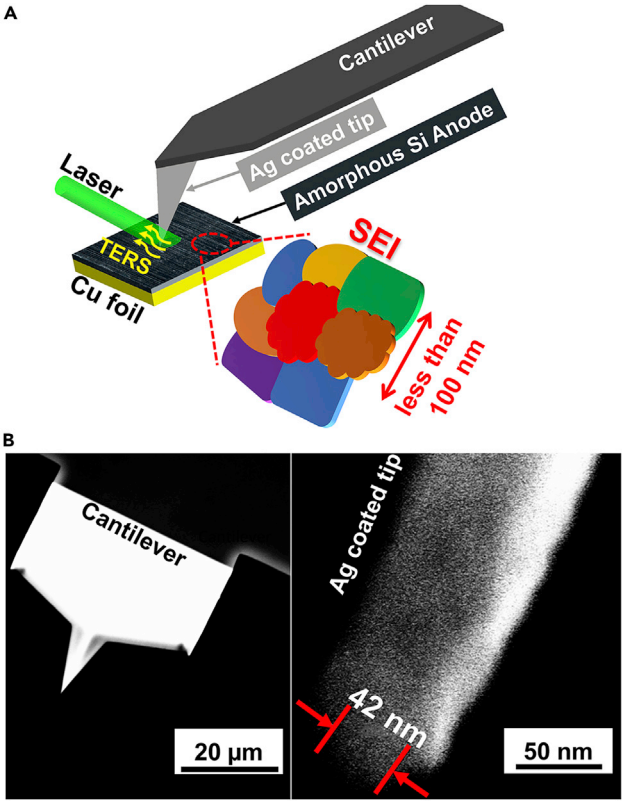

Figure 1. TERS Experimental Setup and Tip Morphology

(A) Schematic illustration of the tip-enhanced Raman spectroscopy (TERS) setup for measuring the SEI on the surface of cycled a-Si with nanoscale in-plane resolution.

(B) SEM micrograph of the cantilever and apex of the silver-coated TERS tip.

SEI has a mosaic-type nano-island structure in the sample plane and a multilayered structure through the sample plane.

RESULTS AND DISCUSSION

Figure 1A illustrates the TERS setup combining the atomic force microscope (AFM) with a confocal side-illumination Raman spectrometer. The confocal plane of the incident laser is focused on the apex of the silver-coated tip. This creates a localized surface plasmon resonance (SPR) at the surface of the tip apex. The SPR provides a greatly enhanced electromagnetic field (EM-field) or "hot spot" in which the probed molecules exhibit strongly enhanced Raman signals in the far field. Figure 1B shows an SEM image of the top-view of the as-coated AFM tip cantilever (left) and the magnified view of the tip apex (right). The tip diameter is ~42 nm, which offers the potential to probe the SEI underneath the tip at nanoscale resolution.

Well-controlled thin films (50 nm) of a-Si were deposited onto copper foil current collectors using radio frequency (RF) magnetron sputtering. Electrochemical characterization of the a-Si anodes can be found in Figure S1. The dominant SEI components evolve over time as cycling proceeds. Samples with low surface roughness are critical for TERS, especially for getting a direct correlation between topography and chemical imaging. The local roughness of the samples studied here ranges between 20 and 500 nm, whereas the AFM topography of an area of $10 \times 10\ \mu m^2$ for each sample exhibits submicron roughness (Figure S2) mainly due to the texture of the copper

Please cite this article in press as: Nanda et al., Unraveling the Nanoscale Heterogeneity of Solid Electrolyte Interphase Using Tip-Enhanced Raman Spectroscopy, Joule (2019), https://doi.org/10.1016/j.joule.2019.05.026

current collector (Figure S3). Previous studies in our group based on the NR suggest that the thickness and the chemical composition of the SEI on a similar a-Si model anode dynamically changed with respect to the lithiation state and cycling.[33] Because of the imperfection of a rough surface on the current model anode a-Si and the severe volumetric changes, it is difficult to probe the thickness heterogeneity of the SEI layer on the a-Si surface after a certain galvanostatic cycle. Further, TERS works ideally on a smooth a-Si surface to reveal the microscale-to-nanoscale heterogeneity of the SEI thickness and its correlation to the local SEI chemistry.

It is worth noting that the SEI formation is by no means a simple process and is in fact influenced by several other factors, such as the state of charge (SoC),[7,33] voltage,[17,34] additives,[35] current rate,[36] temperature,[37] and aforementioned substrate conditions (such as surface roughness). In order to dynamically observe the SEI formation and the associated chemical changes, in operando studies are much more valuable. However, there are significant challenges associated with developing in operando electrochemical TERS (EC-TERS), described later in the text. In this study, we narrow our scope to the nanoscale chemical and structural evolution of the SEI under galvanostatic cycling, while keeping all other conditions the same (see Supplemental Experimental Procedures).

Nanoscale Chemical Heterogeneity of SEI from TERS Mapping

Before a detailed discussion regarding how the TERS results change with respect to cycling, a brief outline of the figure organization is necessary. Figure 2 shows the AFM topography and the TERS intensity mapping of a few individual bands from the principal chemical components of SEI from each a-Si sample. Figure 2 right column shows composite TERS mapping of each sample, providing an overview of the distribution of the vibrational modes representing dominant vibrational species. The topography and chemical imaging are on the same sample area with the spatial resolution given by the scale bar in each map. The intensity of each vibrational signal is given by the color bar, which roughly indicates the surface abundance of each chemical moiety. The vibrational bands and their principal chemical components are summarized in Table 1, which provides a comparative analysis from literature from other spectroscopic methods. To further confirm the TERS vibrational assignment, a detailed comparison between the representative TERS spectra of each sample with the spectra collected from Raman and IR of many model SEI species is shown in Figure S5. In order to highlight the heterogeneous SEI chemical signatures at the nanoscale, 9 spots (denoted by 1–9 in Figure 2, right column) for each a-Si, with each set of three spots 10 nm apart from each other, were selected for detailed spectral analysis as shown in Figure 3.

An immediate observation for 1× a-Si TERS mapping (Figures 2A–2E) is that the distribution of the selected chemical moieties in each TERS map follows the AFM topography, in which the SEI tends to distribute on top of the ridge-like a-Si. This trend is not observed for 5× and 20× samples, which might result from the increasing thickness and roughness of SEI with prolonged electrochemical cycling and the reshaping of the a-Si surface due to enormous volume changes during lithiation (delithiation) (see Figure S6). For 1× a-Si, the band at 740 cm^{-1} is assigned to the –OCO/OCO deformation mode of LEDC.[38] The convolution of $–CH_2$ rocking mode with this band cannot be ruled out in this frequency range.[39] The formation of LEDC stems from the single electron reduction of EC, followed by a combination of two ring-opened EC radicals (Figure 4A). The 740 cm^{-1} band is in accordance with IR bands for LEDC monomer (740 cm^{-1}) and dimers (746 cm^{-1}) as estimated from ab initio quantum chemical calculations by Zhuang et al.[38] The band centered at 1,281 cm^{-1} is the combination mode of

Please cite this article in press as: Nanda et al., Unraveling the Nanoscale Heterogeneity of Solid Electrolyte Interphase Using Tip-Enhanced Raman Spectroscopy, Joule (2019), https://doi.org/10.1016/j.joule.2019.05.026

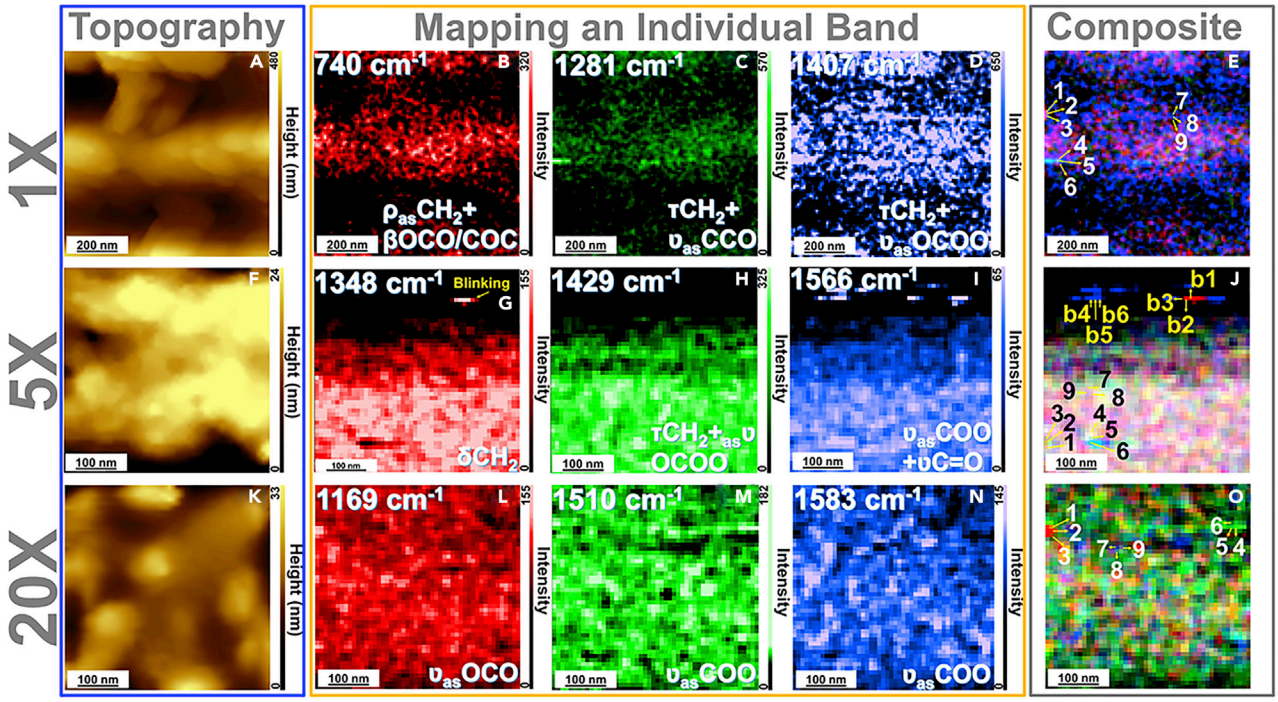

Figure 2. The Combination of AFM Topography, TERS Mapping of an Individual Vibrational Mode, and Composite TERS Maps of Different a-Si Samples

AFM topography (blue box), TERS mapping of an individual band (orange box), and composite TERS maps (gray box) of 1×, 5×, and 20× a-Si samples. The topography and chemical imaging are on the same sample area. The color bar of the AFM topography indicates the relative height. The individual band TERS mapping quantifies the intensity of a band after spectral background correction of each vibrational signal scaled by the false color bar. TERS mapping indicates the overlap of (A) CH_2 rocking, –OCO, and –COC deformation bands (~740 cm^{-1}); (B) –CH_2 twisting and asymmetric CCO stretching bands (1,281 cm^{-1}); and (C) –CH_2 twisting and asymmetric OCOO stretching bands (~1,407 cm^{-1}) collected from 1× a-Si, respectively. For 5× a-Si, TERS mapping respectively shows the combination of (G) –CH_2 bending band (1,348 cm^{-1}); (H) –CH_2 twisting and asymmetric OCOO stretching bands (~1,429 cm^{-1}); and (I) –CH_2 twisting, asymmetric COO stretching, and C=O stretching bands (1,566 cm^{-1}). For 20× a-Si, TERS mapping exhibits the (L) asymmetric –OCO stretching band (1,169 cm^{-1}); (M) bidentate asymmetric –COO stretching band (1,510 cm^{-1}); and (N) the monodentate asymmetric –COO stretching bands (1,583 cm^{-1}). (E), (J), and (O) in the right gray box shows the composite TERS maps for all samples. The number index of the composite map marks where the sample TERS spectrum was taken.

CH_2 twisting and –CCO asymmetric vibration, ascribed to PEO-like oligomer species in the SEI (Figure S5). It is clear that the distribution of the 1,281 cm^{-1} band on 1× a-Si surface (Figure 2C) is different from that of the 740 cm^{-1} band (Figure 2B), indicative of different local distributions of the LEDC and PEO components in SEI at nanoscale. Shown in Figure 2D, the intensity mapping of the 1,407 cm^{-1} peak, ascribed to hybrid modes of CH_2 twisting and –OCOO asymmetric stretching from LEDC,[38,40] shows a different pattern from the former two bands, again confirming the high spatial and compositional heterogeneity of the SEI. Detailed analysis of the 1× a-Si TERS spectra at selected locations is shown in Figure 3A. It is worth emphasizing that even bands that stem from one species in the SEI may have different intensity distributions. The 740 cm^{-1} band of spectra 1–3 are most distinguished (see Figure 3) among other selected spectra. However, the intensity of this band in spectra 4–6 decreases by 6 times, whereas another three bands at 1,281, 1,407, and 1,433 cm^{-1} gain in intensity. The difference in relative intensity of LEDC-associated bands at different locations can be attributed to different orientations of the functional groups with respect to the local electromagnetic (EM) vector field (also see Figure S5). The scattering tensor of a given vibrational mode of a probed molecule, which determines the enhanced Raman intensity, is dictated by the orientation of the molecule versus the local EM vector field.[41] The EM-field under the tip is inhomogeneous at the nanoscale, and the LEDC molecules may have different orientations at these two locations with respect to the EM

Please cite this article in press as: Nanda et al., Unraveling the Nanoscale Heterogeneity of Solid Electrolyte Interphase Using Tip-Enhanced Raman Spectroscopy, Joule (2019), https://doi.org/10.1016/j.joule.2019.05.026

Table 1. TERS Peak Assignment for Different SEI Species of Each a-Si Sample

Number of Cycles	Spectral Position (cm^{-1})	Principal Chemical/ Vibrational Signature of SEI from TERS	Band Assignment
1×	740	LEDC	$\rho_{as}(CH_2)+\beta$(OCO/OCO) Zhuang et al.[38]
	1,281	PEO	$\tau(CH_2)+\nu_{as}$CCO Socrates[39]
	1,407	LEDC	$\tau(CH_2)+\nu_{as}$OCOO Zhuang et al.[38]
	1,433	LEDC	$\tau(CH_2)+\nu_{as}$OCOO Zhuang et al.[38]
5×	1,348	PEO/LEDC	$\delta(CH_2)$ Zhuang et al.[38] and Socrates[39]
	1,429	LEDC	$\tau(CH_2)+\nu$COO Zhuang et al.[38]
	1,491	LEDC	$\chi(CH_2)$ Zhuang et al.[38]
	1,566	LEDC	ν_{as}(COO)+ν(C=O) Zhuang et al.[38]
	1,588	LEDC	ν_{as}(OCO) Zhuang et al.[38]
	822	R_2POF	ν(PF) Yoon et al.[37]
	929	$RPOF_2$	ν(PF) Yoon et al.[37]
20x	1,169	LEDC	ν_{as}(OCO) Zhuang et al.[38]
	1,460	monodentate carboxylate	$\omega(CH_3)$ Socrates[39]
	1,510	bidentate carboxylate	ν_{as}(COO) Socrates[39]
	1,565	bridging + monodentate carboxylate	ν_{as}(COO) Socrates[39]
	1,583	monodentate carboxylate	ν_{as}(COO) Socrates[39]
	1,632	monodentate carboxylate	ν_{as}(COO) Socrates[39]

vector, thereby differentiating the EFs for various vibrational modes. Banik et al. reported that the EF of dibenzyldithio in the gap of two adjacent Ag nanoparticles varied by more than an order of 4 among vibrational modes of different relative orientations to the EM-field.[41] It is also worth noting that the abundance of band intensity related to species A with respect to the bands of species B indicates the local distribution preference of species A over B. Seen from Figure 3, the 1,281 cm^{-1} band decreases in intensity in spectra 3–6 with respect to that of the spectra 7–9, again indicating that PEO preferably distributes in spot 3–6. The local abundance of the vibrational mode should not be related to the global abundance of the related species. Alison et al. used selective ^{13}C labeling and solid-state NMR to confirm that >50% of the decomposition products on Si using an EC-DMC electrolyte were PEO,[34] stemming from the multiple electron reduction of EC (Figure 4B). A composite TERS map for 1× a-Si better illustrates the nanoscale heterogeneous distribution of the SEI composition (Figure 2, right top). Notably, besides the locations showing magenta color (red and blue mixture) mostly on the Si ridge (see Figure 2A), spots of individual color of blue or red are concentrated on several locations (at the Si-ridge rim). Likewise, this is due to the various orientations of the LEDC with respect to the EM-field vector underneath the tip apex.[41] More details can be found in the Supplemental Information.

Shown in Figures 2F–2J, we demonstrate that LEDC is the more dominant species in the SEI for the 5× a-Si, and the AFM topography is not as well correlated to the TERS mapping as for 1× a-Si. This trend may be initiated earlier than the 5^{th} cycle, as indicated by the TERS mapping and the AFM topography of the 3× a-Si (Figure S8). AFM topography and TERS maps of three different vibrational modes of the 5× a-Si (Figures 2G–2I), namely $–CH_2$ bending (1348 cm^{-1}), hybrid of $–CH_2$ twisting and –OCOO stretching (1,429 cm^{-1}), and the hybrid of asymmetric –COO stretching and C=O stretching (1,566 cm^{-1}) are shown in Figure 2, middle row. The first band stems

Please cite this article in press as: Nanda et al., Unraveling the Nanoscale Heterogeneity of Solid Electrolyte Interphase Using Tip-Enhanced Raman Spectroscopy, Joule (2019), https://doi.org/10.1016/j.joule.2019.05.026

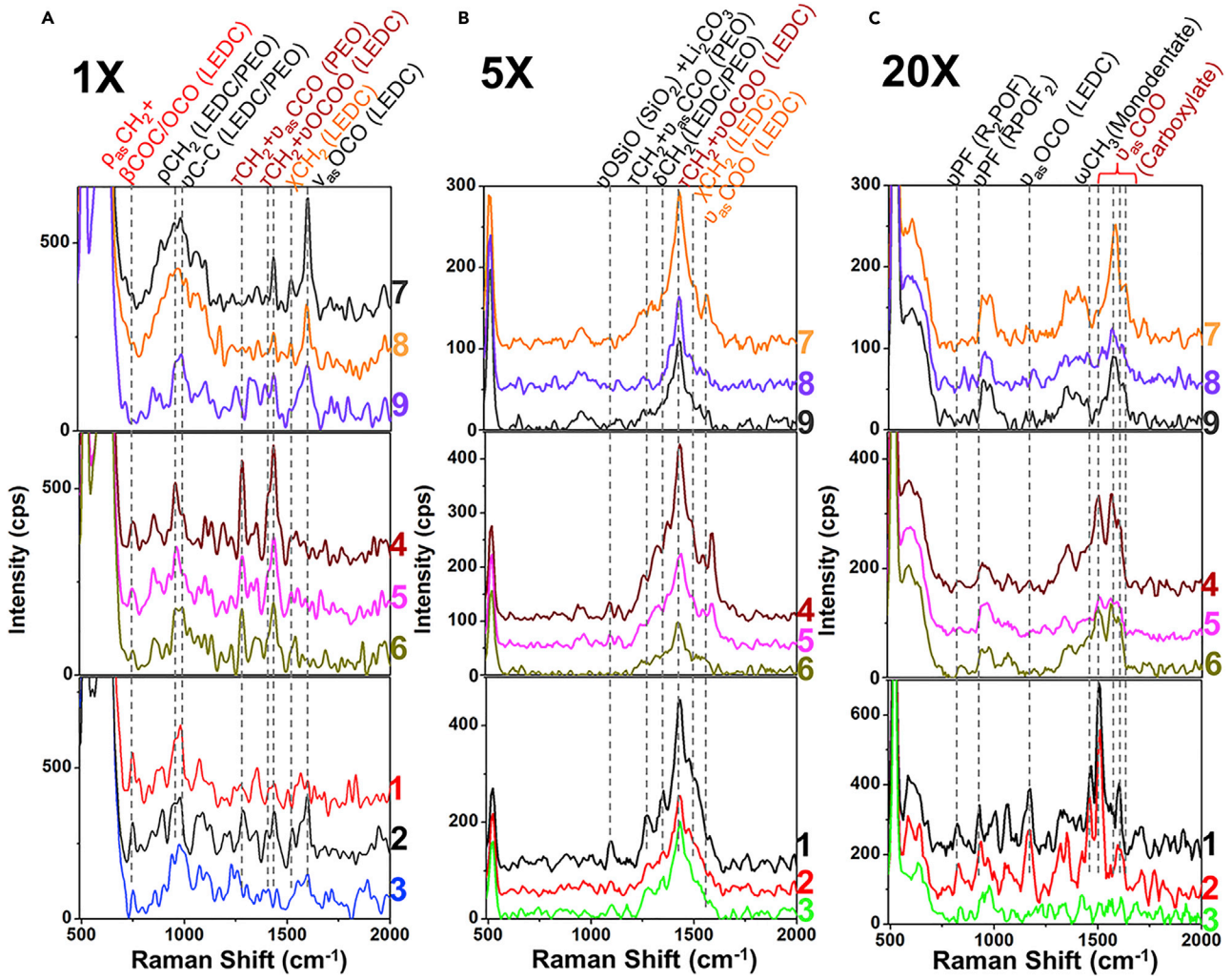

Figure 3. TERS Spectra Obtained from Different Locations of Each a-Si Sample

TERS spectra collected from various locations of (A) 1× sample, (B) 5× sample, and (C) 20× sample. The assignment for bands of interest is at the top of each plot. For a full frame of the peaks around 500 cm^{-1}, which stem from the tip Si or a-Si anode, readers may resort to Figure S7. The Greek symbols denote corresponding vibrational modes for ν, stretching; δ, bending; χ, scissoring; τ, twisting; ρ, rocking; β, deformation; and ω, wagging.

from PEO oligomer or LEDC, and the latter two are from LEDC monomer or dimer.[38] Notably, a parallel line pattern shows up in the 1,348 and 1,566 cm^{-1} maps. More detailed inspection of the spectra taken from the line pattern (spot b1 to b6 in the combined TERS mapping) indicates that the corresponding bands are of much higher TERS intensity (up to 7-fold increase) than those taken from other places (Figure S9), attributed to the TERS "blinking" phenomenon in which extreme TERS intensity of probed species shows up intermittently.[42] Nine spectra of high intensity of each corresponding band were taken from spot 1 to 9 and plotted in Figure 3. An immediate observation is that the peak centered at 1,429 cm^{-1} dominates in all spots, close to the –OCOO symmetric stretching mode and the $–CH_2$ twisting as reported for the LEDC monomer at 1,427 cm^{-1}.[38] It is worth mentioning that the 1,427 cm^{-1} band shall not be assigned to Li_2CO_3, which has an admixture of transverse optical (TO) and longitudinal optical (LO) modes at 1,420 cm^{-1} for Raman and 1,460 cm^{-1} for IR, as reported by Bates et al.[43] The Raman intensity of this band, however, is only 4% of that at 1,091 cm^{-1} (a band shown in Figure 3, bottom). Thus, this band should

Please cite this article in press as: Nanda et al., Unraveling the Nanoscale Heterogeneity of Solid Electrolyte Interphase Using Tip-Enhanced Raman Spectroscopy, Joule (2019), https://doi.org/10.1016/j.joule.2019.05.026

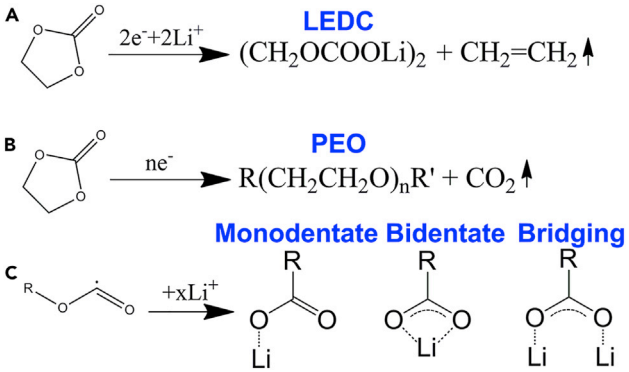

Figure 4. Scheme of Possible Reaction Paths to Form the Various SEI Components on a-Si

(A) The generation of LEDC from the double-electron-reduction reaction of EC.

(B) The generation of PEO from the multiple-electron-reduction reaction of EC.

(C) The formation mechanism of various carboxylate conformations.

be exclusively assigned to LEDC. Evidently, LEDC dominates the TERS spectra of all spots chosen from 5× a-Si. This finding is further evidenced by a small shoulder shown at 1,491 cm^{-1} (–CH_2 scissoring, χ) and a weak band centered at 1,588 cm^{-1} (–OCO asymmetric stretching) from the LEDC dimer or monomer.[38] The existence of other components such as PEO, $LiSiO_x$[40], and Li_2CO_3 cannot be ruled out. The combined TERS mapping of 5× a-Si (Figure 2, right middle) does not show distinguished correlation to the topography of the same sample, indicating that the spatial distribution of the SEI chemical information from TERS deviates from the AFM's height profile. More importantly, bands assigned to LEDC monomer-dimer show that TERS is a unique tool for depicting the vibrations of the local SEI species on the molecular level. It is worth noting that, the TERS measurements on the 3× a-Si sample present a transition stage between 1× a-Si and 5× a-Si (Figures S5 and S8).

For 20× a-Si, the local dominant species evolves into carboxylate (RCO_2Li) compounds (including polycarbonate) and fluorinated species ($Li_xPO_yF_z$). The most exciting findings of the SEI on the 20× a-Si surface are that the intrinsically unobservable –COO stretching related Raman modes become active for TERS, and the small variation of the band centers for these modes indicates the molecular conformational change in outer layer of the SEI, which cannot be readily detected by other characterization methods.

The TERS mapping and spectra of –OCO asymmetric stretching (1,169 cm^{-1}), bidentate –COO asymmetric stretching (1,510 cm^{-1}), and monodentate –COO asymmetric stretching (1,583 cm^{-1}) are shown in Figures 2 and 3. While the first band stems from the LEDC, the Raman intensity from other LEDC featured bands decreases as compared with the 5× a-Si samples (see Figures 3B and 3C). Several vibrational modes between 1,450 and 1,650 cm^{-1} gain in intensity, which cannot be assigned to either PEO or LEDC as observed in the case of 1× and 5× samples (also see Figure S10). Additional TERS mapping measurements on several different locations of two 20× a-Si samples consolidate our observations on the multiple vibrational modes in this frequency region, as shown in Figure S11.

The multiple –COO stretching modes may stem from the carboxylate compounds (RCO_2Li),[39] which are formed either by thermal decomposition of the LEDC over prolonged galvanostatic cycling[37] or by ester radicals coordinating to Li^+[44] as illustrated in the reaction scheme (Figure 4). It is quite possible that after the extended

Please cite this article in press as: Nanda et al., Unraveling the Nanoscale Heterogeneity of Solid Electrolyte Interphase Using Tip-Enhanced Raman Spectroscopy, Joule (2019), https://doi.org/10.1016/j.joule.2019.05.026

galvanostatic cycling, the a-Si SEI may also contain polycarbonate species, similar to what has been observed for the graphite anode after prolonged cycling.[6,45] Since polycarbonate compound presents similar vibrational modes as small carboxylate molecules, it is hard to differentiate their TERS spectra. Previous vibrational assignment in this frequency range relies only on IR spectroscopy.[37,40,46] However, those bands were not well spectrally resolved and explained, possibly because of the low IR absorbance for the carbonate compounds in this frequency region (details in Figure S5). To our best knowledge, the Raman vibrational modes in this frequency region for the carbonate compounds in SEI have not been reported. A detailed comparison between Raman and IR spectra of the model carbonate species, including lithium carbonate and lithium acetate (Figure S5) indicates that the –COO stretching modes above 1,450 cm^{-1} are only IR active but not Raman active. The fact that the –COO stretching modes are Raman active in TERS configuration stems from the difference between the surface selection rule and the selection rule for the normal Raman vibrations (Figure S5).

Another interesting point worth noting is that the exact band centers of the –COO stretching modes between 1,450 and 1,650 cm^{-1} slightly vary on different locations (see Figures 3C and S11; Table S1). This should result from the surface molecular conformational change of the carboxylate compounds. It is almost impossible to perform spectroscopic measurements on the carboxylate compounds of only a single molecular conformation. Therefore, to provide further confirmation, using a simple carboxylate compound, lithium acetate as a model, we carried out molecular dynamics (MD) simulations and DFT calculations for three different carboxylate conformations. The calculated Raman spectra and the experimentally measured TERS spectra were compared and shown in Figure 5. The TERS spectrum taken from spot 1 has a featured band at 1,510 cm^{-1} and a satellite band at 1,460 cm^{-1}, in accordance with the calculated asymmetric –COO stretching mode from the bidentate carboxylate (ca. 1,517 cm^{-1}) and the $–CH_3$ wagging mode from the monodentate carboxylate (ca. 1,454 cm^{-1}), respectively (Figure 5B).[39] The analysis of the lower frequency bands indicates that the acetate ions are less coordinated to the Li^+ cation (Figure S10). In spectrum 4, the broad peak centered at 1,565 cm^{-1} may be ascribed to a convolution of the asymmetric –COO stretching of bridging (ca. 1,552 cm^{-1}), bidentate, and monodentate structures (ca. 1,584 cm^{-1}). Spectrum 8 exhibits two distinguished bands at 1,583 and 1,632 cm^{-1}, both of which are ascribed to the monodentate asymmetric –COO stretching mode. The origin of the subtle difference of these two vibrational modes could be rationalized by considering local intermolecular interactions. In Figure 5B, DFT calculation indicates that the lower frequency band stems from the asymmetric movement of the coordinated (with Li^+) oxygen toward the central Li^+ (denoted as I.υ_{asCOO}), whereas the higher frequency band corresponds to the symmetric movement of the surrounding oxygen oscillating toward the central Li^+ (denoted as II.υ_{asCOO}). Other contributions to the –COO vibrational shift include the free carboxylate ions with respect to those that coordinated to the Li^+ cation (Figure S10), the different molecular orientations with respect to the local EM-field vector, and the non-coincident effect stemming from the resonant vibrational coupling between molecules.[47]

The fluorinated species were also on the outer shell of the SEI layer of the 20× a-Si. This is evidenced by a band centered at 822 cm^{-1} (P-F stretching in $–R_2POF$) and another at 929 cm^{-1} ($RPOF_2$ stretching). These vibrational modes indicate the existence of $Li_xPO_yF_z$ in the Si SEI,[37] which may result from the reduction of the $LiPF_6$ salt. The increase of fluorinated species in SEI with respect to the cycling number is further confirmed by the element composition analysis from EDX mapping (Figure S12).

Please cite this article in press as: Nanda et al., Unraveling the Nanoscale Heterogeneity of Solid Electrolyte Interphase Using Tip-Enhanced Raman Spectroscopy, Joule (2019), https://doi.org/10.1016/j.joule.2019.05.026

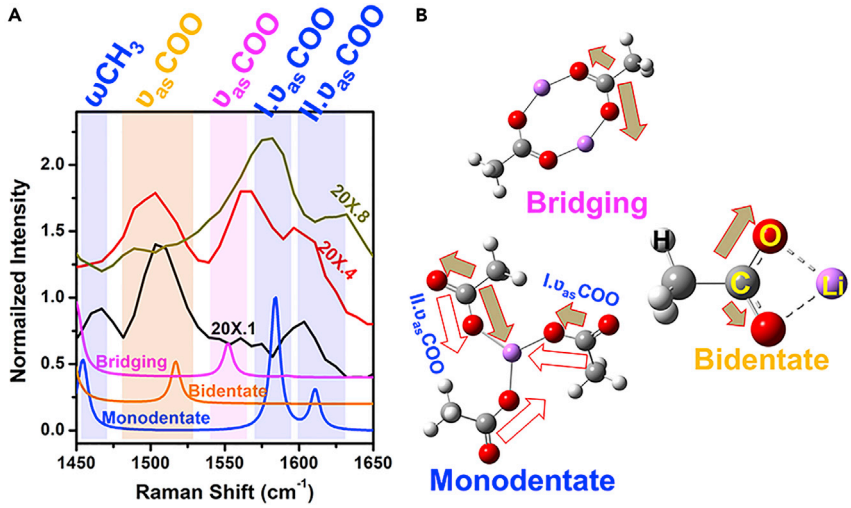

Figure 5. Comparison between the TERS Spectra with These Calculated by DFT of Various Carboxylate Conformations

(A) Comparison between normalized TERS spectra taken from various locations (8, 4, and 1 of Figure 3C) of the 20× a-Si surface and simulated Raman spectra for bridging, bidentate, and monodentate conformations. The number used to identify each spectrum is in accordance to the spectrum in Figure 3C.

(B) Three conformations of the carboxylate compounds coordinated with Li^+. Gold arrows indicate –COO symmetric stretching modes for monodentate (blue), bidentate (orange), and bridging (magenta) conformations, respectively.

The aforementioned TERS vibrational modes were compared with Raman and IR spectra of several commonly seen model SEI species as shown in Figure S5. It is worth re-emphasizing that the activity of the vibrational modes differs for various molecules within the SEI. And the spectroscopic selection rules vary for surface-enhanced Raman (i.e., TERS in this case),[48] standard confocal Raman spectroscopy, and IR (see Supplemental Information for details). While more accurate assignment of the TERS vibrational modes necessitates further TERS studies on well-defined model SEI molecules on a delicately prepared substrate, our groundwork of analysis on the TERS vibrational modes on the a-Si SEI of complicated chemistry is generally satisfying. We need to mention that the laser power used in the current study was only 25 μW, much smaller than that needed for standard confocal micro-Raman measurements on the SEI layer (milliwatts level).[49]

It is also worth noting that SEI formation dynamics should ideally be studied under in operando conditions. However, the current proof-of-concept EC-TERS setup has only been successfully applied to model molecular systems with a narrow voltage window (e.g., < 0.8V versus Ag/AgCl) in aqueous solutions.[50–52] The major technical hurdles for in operando EC-TERS includes the liquid-induced optical distortion of the laser illumination, the high standards for a proper optical design and potential control over the working electrode,[53] and the reproducible TERS tips that can survive the harsh environment of the corrosive carbonate electrolytes and be stable over a broad voltage window versus Li/Li^+.

Based on the TERS analysis, Figure 6 schematically summarizes the SEI evolution as a function of galvanostatic cycling of a-Si. For cycled a-Si, 1× a-Si has rich local SEI species of PEO-like oligomer and LEDC, whereas the SEI on 5× a-Si is dominated by the LEDC species. The SEI on 20× a-Si is enriched in carboxylate compounds, which have several different molecular conformations.

Please cite this article in press as: Nanda et al., Unraveling the Nanoscale Heterogeneity of Solid Electrolyte Interphase Using Tip-Enhanced Raman Spectroscopy, Joule (2019), https://doi.org/10.1016/j.joule.2019.05.026

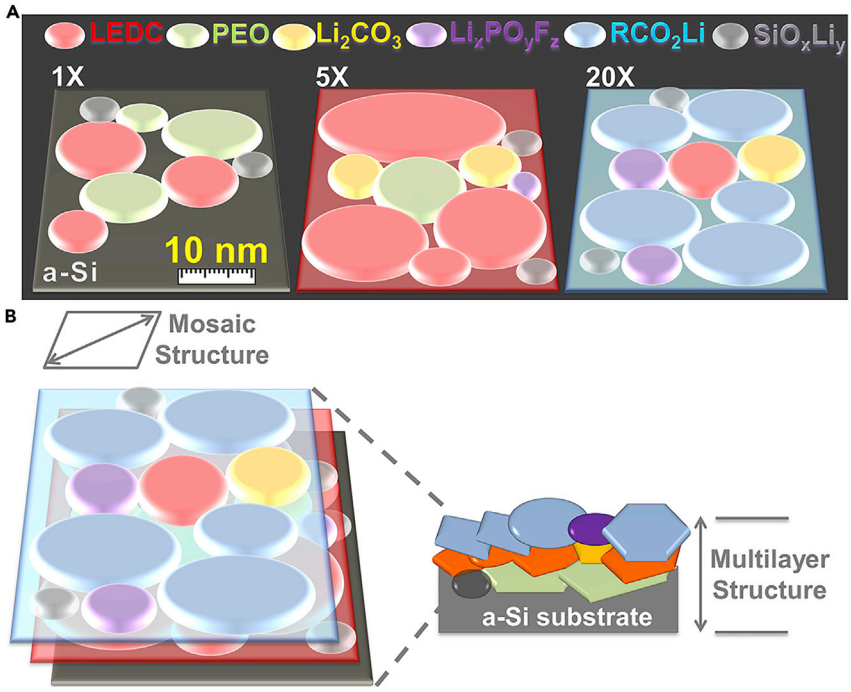

Figure 6. Schematic Illustration of the Nanomosaic-Multilayer Hybrid SEI Model

(A) Schematic of the SEI tomography evolution with respect to the increasing galvanostatic cycle number probed by TERS.

(B) Schematic of the proposed SEI structure on cycled a-Si surface.

Different than other vibrational spectroscopic technologies, such as confocal Raman microscopy and IR, TERS is only sensitive to a less than 5 nm layer on the SEI surface (Figure S13). On this basis, it is clear from Figure 2 that the composition has a mosaic-type structure on each of the cycled a-Si anodes across the sample plane. Because of the fact that the SEI composition varies with respect to the galvanostatic cycling, it is most likely that the SEI has a layered structure through the sample plane, with each layer enriched in different chemical species. After prolonged cycling, the outer layer of the SEI is rich in carboxylate compounds, and the carboxylates have various molecular conformations because of their different ways of coordination to Li^+ cations. In this context, we propose a nanomosaic-multilayer hybrid structure for the SEI on top of the a-Si thin film anode, as illustrated in Figure 6. From the SEI formation dynamic perspective, it is highly possible that various side reactions (e.g., a few of these reactions are listed in Figure 4) concurrently occur on a number of active sites on top of the a-Si several nanometers away from one another, which seed the local SEI growth. These side reactions have various preferred reaction kinetics at a different stage of cycling of the a-Si so as to generate different abundances of the SEI components locally. It is important to note that the proposed SEI model is based on chemical information depicted by TERS (or Raman) active modes. A more comprehensive model can be built by combing with other complimentary techniques, which would be a topic for future study.

PCA-MCR Analysis of TERS

The TERS mapping and analysis discussed so far is based on single or individual spectral changes corresponding to specific vibrational modes. Such monovariant characterization is not a good statistical measure to capture the changes in vibrational band distribution of different SEI chemical species. More quantitative analysis

Please cite this article in press as: Nanda et al., Unraveling the Nanoscale Heterogeneity of Solid Electrolyte Interphase Using Tip-Enhanced Raman Spectroscopy, Joule (2019), https://doi.org/10.1016/j.joule.2019.05.026

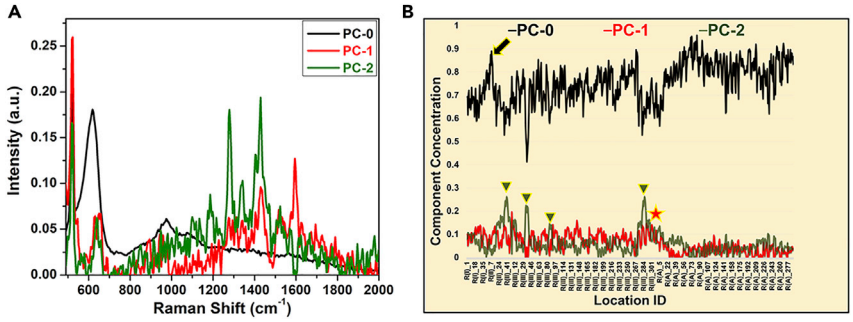

Figure 7. The Statistical Analysis of the TERS Spectra from 1× a-Si Based on PCA and MCR

(A) The pure spectral components derived from PCA-MCR analysis.

(B) The abundance of the pure component represented by the component concentration in selected regions with designated location IDs. Resort to Figure S15 for location ID details.

in TERS spectra with differing locations across each a-Si surface can be obtained from PCA and MCR of the TERS spectra.[54] PCA determines the smallest number of pure spectral components (PCs) needed in linear combination to obtain the sample spectral variation (Figure S14). Subsequently, pure component spectra are extracted by MCR using alternating least-squares curve fitting. In this way, information contained in the large spectral set is projected onto a smaller number of latent variables. The three pure spectral principle components (PC-0 to PC-2) derived from the TERS spectra of 1× a-Si and their concentrations in different regions are shown in Figure 7. The TERS spectra were chosen from several different locations for PCA-MCR analysis on each a-Si sample (see Figure S15 for detailed location ID assignment).

An immediate observation from Figure 7B is that the principal component 0 (denoted as PC-0) almost dominates all locations selected from a-Si in Figure 7B (also see Figure S15, with the spectral concentration larger than 60% in most spots). PC-0 for 1× a-Si has a featured band at 622 cm^{-1} (assigned to lithiated a-Si, Figure S7) and a broad band centered at 973 cm^{-1} (assigned to Si-O stretching), which clearly suggests that the probed area of the 1× sample was only partially covered by SEI or the SEI is too thin to contribute to a distinguishable spectral signal. A few locations have a PC-0 distribution >85% (e.g., R(II)_7 marked by an arrow in Figure 7B). This may suggest an even sparser SEI distribution. PC-1 has two prominent bands at 1,433 and 1,595 cm^{-1}, indicative of the distribution of LEDC and carboxylate species. The spectral abundance of PC-1 is lower than 10% for most locations indicative of <10% abundance of the LEDC-carboxylate composite species in the probed locations. Exception exits in a few spots where the abundance of PC-1 is larger than 10% (e.g., pentacle marked region in Figure 7B). Two featured bands at 1,279 and 1,429 cm^{-1} are observed for PC-2, corresponding to the PEO and LEDC species. The proportion of PC-2 is lower than 10% for most locations but larger than 15% at locations R(II)_22 to 45, R(III)_33 to 41, R(III)_80 to 97, and R(III)_272 to 299, with the maximum value of 26% found at R(II)_40 (these locations were marked by the triangles in Figure 7B). This is in good agreement with the TERS mapping analysis, where PEO-like oligomer and LEDC distributes preferably in the SEI on 1× a-Si, and the distribution of the components is highly heterogeneous.

The PCA-MCR analysis on 5× and 20× a-Si samples (Figure S15) indicates that the dominant species in most locations are LEDCs and carboxylate compounds, respectively. Overall, the semi quantitative PCA-MCR analysis on the original TERS spectra

Please cite this article in press as: Nanda et al., Unraveling the Nanoscale Heterogeneity of Solid Electrolyte Interphase Using Tip-Enhanced Raman Spectroscopy, Joule (2019), https://doi.org/10.1016/j.joule.2019.05.026

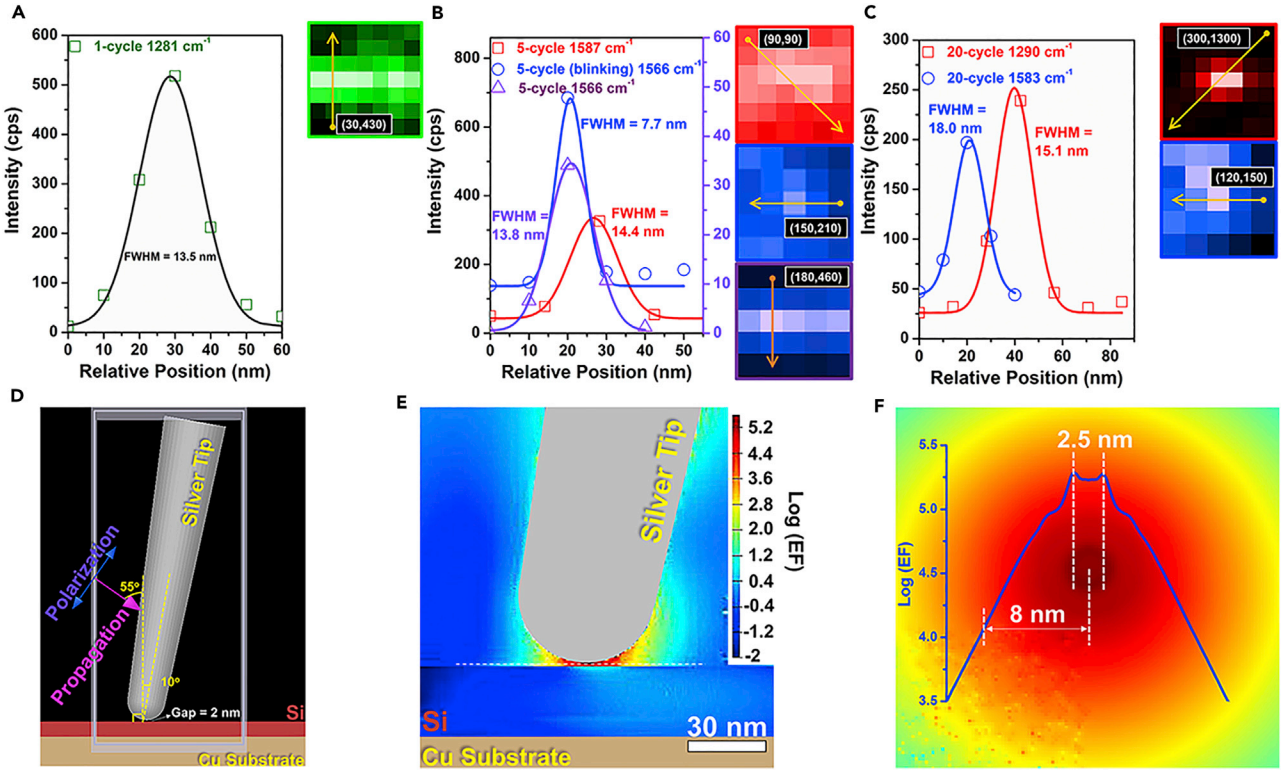

Figure 8. The Consolidation of In-plane Nanoscale Resolution for TERS

(A–C) The in-plane spatial resolution evaluation for (A) 1× a-Si, (B) 5× a-Si, and (C) 20× a-Si at various locations and line cut directions. Each plot stands for the intensity cross section of the related band along the arrowed line. The corresponding TERS intensity images were taken from different locations of each sample. The dot in each orange arrow stands for the origin of the line cut position, labeled by its absolute Cartesian coordinate.

(D–F) Finite difference time domain (FDTD) simulation based on the current TERS setup. (D) The FDTD model setup. Detailed description of the FDTD model setup can be found in the Experimental Procedures. (E) Simulated enhancement factor (EF) distribution. Maximum EF concentrates between the tip apex and the silicon surface to form a ring structure. (F) The 2D EF distribution on the central plane indicated by the dash line in (B). The blue curve indicates the EF distribution along the horizontal line cut through the center of the max EF ring.

taken from multiple selected locations is in excellent agreement with the analysis from the individual bands for each a-Si. The PCA-MCR analysis provides more comprehensive reflection and a more direct way of characterizing the general spectral pattern and their abundances distributed on various locations.

Spatial and Spectral Resolution

To acquire the spatial resolution of TERS in our experiments conducted on cycled a-Si, line profiles of various band intensity on different a-Si samples along the arrowed lines marked on the TERS map are fitted by the Gaussian function (Figures 8A–8C). The profile of 1,281 cm^{-1} band (τ_{CH2} + υ_{CCO}) intensity of 1× a-Si along the arrowed line shown in Figure 8A has full width at half maximum (FWHM) of 13.5 nm, which is smaller than the tip diameter (42 nm), comparable with the spatial resolution reported in most AFM-TERS literature.[55] Different band intensity profile along the arrowed line cut of various directions taken from 5× a-Si (Figure 8B) and 20× sample (Figure 8C) presents FWHM between 13.8 and 18 nm, further demonstrating that the spatial resolution is not limited by the overall tip diameter.[53] To further explore the relationship of the size of the EM-field versus that of the tip apex, finite difference time domain (FDTD) simulation was performed (Figures 8D–8F). The FDTD model (Figure 8D) was built per the geometric relation of the

Please cite this article in press as: Nanda et al., Unraveling the Nanoscale Heterogeneity of Solid Electrolyte Interphase Using Tip-Enhanced Raman Spectroscopy, Joule (2019), https://doi.org/10.1016/j.joule.2019.05.026

TERS experimental setup. The 2 nm-gap between the tip and sample is the lowest value when the tip is closest to the sample surface under tapping mode. Figure 8E demonstrates that the EM-field (quantified by EF) is intensified between the tip and substrate. A more quantitative analysis on the EF distribution on the central plane (1 nm away from the sample surface) is shown in Figure 8F. The largest EF value of 2×10^5 centers in a 2.5 nm range. This value decreases to $\sim 10^4$ at the radial distance 8 nm from the tip-sample gap center, in agreement with the experimental observations discussed above. The EF value in the current TERS setup was calculated at 2.7×10^4 based on a "tip-in-tip-out" test (Figure S17), one order of magnitude smaller than the maximum EF at the tip-sample center. We speculate that the disparity arises because FDTD calculates the maximum EF value whereas the TERS experiment averages EF underneath the tip apex (the EF averaged over all meshes on the central plane between the Si surface and the tip apex was estimated at 2.1×10^3) Another reason may be due to the tip blocking a certain amount of excitation light and the Raman signal from the side-illumination setup.

To conclude, our results demonstrate the first TERS study of SEI providing both topographical and chemical mapping of a-Si at nanoscale with extremely high sensitivity and surface selectivity, in contrast to ensemble-averaged information obtained from bulk spectroscopic techniques such as Raman and IR. TERS analysis of 1×, 3×, 5×, and 20× cycled a-Si anodes shows that SEI composition gradually evolves with progressive cycling. The dominant SEI species at probed areas are LEDC and PEO-like oligomers for 1× a-Si, LEDCs for 5× a-Si, and carboxylate compounds for 20× a-Si. Because of its high EF (>104) and excellent spectral resolution, conformational change of the SEI species, such as carboxylate compounds at various locations can be depicted by TERS, confirmed by DFT calculations. Moreover, using the single variant analysis (i.e., single Raman band intensity), the semi quantitative PCA-MCR approach makes it possible to statistically extract and quantify the principal spectral components from a large volume of TERS spectra, which allows a more precise description of the distribution of the SEI components. A good correspondence is found between the SEI film topography and chemical fingerprint for 1× a-Si, while this was not the case for 5× and 20× a-Si. This difference can be attributed to the increasing thickness and roughness of SEI with increasing electrochemical cycling due to significant volumetric expansion (contraction) of the a-Si surface. The analysis of SEI film morphology and composition from TERS provides rich information about the chemical stability, structure, and dynamics at a nanometer precision, which is expected to help reveal more detailed SEI formation and evolution and capacity fading mechanism and aid the precise modification of the structure and components of SEI. The TERS results and analysis discussed for cycled a-Si can be broadly applicable for a number of other redox chemistries where there are kinetically stabilized phases forming reactive interphases, such as Na-ion, solid-state, and metal air chemistries. This is an example where multi-modal spectroscopy such as TERS can provide a useful mechanistic link between nanoscale morphology, interfacial transport, and the overall electrochemical performance.

EXPERIMENTAL PROCEDURES

a-Si Anode Preparation

The pristine amorphous Si (a-Si) anode was prepared by RF magnetron sputtering Si onto a copper foil, which served as the current collector. The film thickness was 50 nm as measured by a quartz-crystal microbalance (QCM). The a-Si-on-Cu foil was dried under vacuum at room temperature overnight before being transferred

into an Ar-filled glove box and punched into disks (1/2″ in diameter). The coin cells (stainless steel CR-2032, Hohsen Corp., Osaka, Japan) were assembled using the a-Si-on-Cu disk as the working electrode, a Li disk (1/2″) as the counter electrode, and a polypropylene membrane (Celgard 2400) as the separator. The electrolyte was lithium hexafluorophosphate ($LiPF_6$, 1M) in ethylene carbonate (EC) and diethyl carbonate (DEC) 1:1 by volume (Sigma Aldrich, battery grade). The cells were cycled at 25°C at 1.93 × 10^{-3} mA/cm^2 (equivalent to C/10 rate) between 1.5 V and 20 mV for the designated number of cycles using a potentiostat (Bio-logic, VMP3). After cycling, the a-Si anode was immediately taken out from the coin cell in the delithiated state in an Ar-filled glovebox (O_2 < 0.1 ppm and H_2O O_2 < 0.1 ppm). The anodes were gently rinsed in triplicate using DEC (Sigma Aldrich, ≥ 99%). The excess liquid was carefully removed by placing a piece of single-ply KimWipes on the edge of the a-Si sample, followed by drying in the glovebox for a minimum of 24 h before all measurements. No residual electrolyte or DEC eluent was observed from the TERS spectra (Figures S18 and S19).

TERS Setup and Raman Measurements

The TERS tips were fabricated by physical vapor deposition (PVD) on commercial AFM tips (Bruker, OTESPA-R3, resonance frequency = 300 kHz, spring constant = 26 N/m, and tip apex diameter = 7 nm). Sequential deposition of chromium (Cr) (adhesion layer, 2 nm), silver (Ag) (plasmonic layer, ~40 nm), and aluminum (Al) protection layer, 2 nm) were performed. Al layer converts to a dense alumina layer that provides good mechanical and chemical protection without significant influence on optical properties of the tip.[56,57] TERS tip fabrication details can be found in Agapov et al.[56] and Barrios et al.[57] The TERS measurements were performed on an atomic force microscope (AFM, AIST-NT SMART PROBE) in connection with a Raman spectrometer (HORIBA Co., Xplora) in an argon-filled environmental control chamber (see Figure S20 for details). Each sample was sealed individually in a gas-tight scintillation vial (20 mL) and transferred from sample-preparation glovebox to the TERS glovebox air free. For TERS measurements, the 532 nm laser wavelength was chosen with a local power of 25 μW. The local laser power was set to 2 mW for standard confocal Raman measurements, with accumulation time set for 120 s. The grating number was 600 grooves/mm, and the objective was 100× (N.A. = 0.7). The following chemicals were used as the model SEI species for the standard Raman measurements. Tetraethylene glycol dimethyl ether (TEGDME, ≥99%), lithium hydroxide powder (LiOH, reagent grate, ≥98%), lithium oxide powder (Li_2O, 97%), lithium carbonate (Li_2CO_3, 99.99% trace metals basis), and lithium acetate (99.95% trace metals basis) were purchased from Sigma Aldrich. Lithium fluoride (LiF, >98%) was purchased from Alfa Aesar. For AFM, the tapping mode was chosen with oscillation amplitude of 20 nm and ~2 nm minimum distance from the sample surface. The mapped area was set at 1 × 1 μm^2 or 500 × 500 nm^2 for each sample with a step size of 10 nm. The accumulation time was 0.5 s for each spectral acquisition. Each frame of the TERS map represents the intensity (after background correction) of the corresponding vibrational mode that arises from functional groups in the SEI components.

FTIR and SEM

The IR spectrum of each sample was collected using an FTIR spectrometer (Bruker, ALPHA) with a diamond attenuated total reflection (ATR) accessory in an Ar-filled glove box. Spectra were collected in the region between 4000 and 650 cm^{-1} (64 scans, 2 cm^{-1} resolution). Scanning electron microscopy (SEM) was used to image the a-Si anodes using a cold-cathode field-emission (FE) SEM system (Hitachi S4800, 20 kV beam voltage, 20 μA beam current). The elemental composition of the Si anode surface was characterized using energy dispersive X-ray spectroscopy

Please cite this article in press as: Nanda et al., Unraveling the Nanoscale Heterogeneity of Solid Electrolyte Interphase Using Tip-Enhanced Raman Spectroscopy, Joule (2019), https://doi.org/10.1016/j.joule.2019.05.026

(EDX) (20 kV, 20 μA). The EDX maps were analyzed by an EDAX Genesis software package.

FDTD Simulations

To better assess the plasmonic properties of the TERS tip and the EM-field distribution, three-dimensional (3D) FDTD simulations (Lumerical Solutions, Inc.) were performed for the TERS setup. Shown in Figure 8D, a silver tip of the diameter at the apex of 42 nm was set 2 nm away from a silicon layer coated on the copper surface. The tip axis forms an angle of 10° with the sample plane vector. A plane wave of electric field, E, polarized along the blue double-arrow in Figure 8D propagates along the vector (marked by a pink arrow), of 55° with the silicon sample plane. The wavelength of the plane wave was set at 532 nm. The discretized spatial mesh size was 0.1 nm. The perfectly matched layer (PML) boundary condition (BC) was set for all edges of the simulation box (author may resort to the supporting information of the reference for mathematical details of the PML BC). The gap between the tip apex and silicon surface is 2 nm. The optical constants of all materials in this study were referenced from the tabulated values reported in Johnson and Christy.[58]

DFT Calculations

Theoretical Raman spectra were calculated using cluster-based DFT calculations for comparison within the Gaussian (G16)[59] suite of programs. Becke's three-parameter hybrid method using the Lee–Yang–Parr correlation functional (B3LYP)[60] was chosen in this study. Geometries were optimized and vibrational modes as well as Raman intensities were calculated in G16 at B3LYP/6-31+G(d) level of theory. Frequencies are computed by determining the second derivatives of the energy with respect to the Cartesian nuclear coordinates and then transforming to mass-weighted coordinates. Acetates are selected as model molecules for carbonyl (–COO) group containing components in SEI, and three structures are modeled as representatives for monodentate, bidentate, and bridging conformations to study the difference in characteristic –COO vibration modes. The -CH_3 bending band was chosen as the reference position to validate the calculation method as it lies right aside the interested –COO stretching band. The calculated CH_2 bending frequencies are around 1,397 cm^{-1}, suggesting a scaling factor of 0.965–0.968 to match the calculated frequencies to the experimental value at 1,354 cm^{-1} when using the lithium carboxylate -CH_3 bending Raman mode as a reference (Figure S21), which agrees with the factor of 0.963 recommended for this level of calculations. Therefore, this level of theory can adequately predict the interested band area, and 0.965 was used as the scaling factor for band frequencies in the present work.

PCA and MCR

The PCA implemented in the Unscrambler uses the "nonlinear iterative partial least square" (NIPALS) algorithm. Details are described in Martens and Naes.[61] The mutually orthogonal pure component matrix, l_i, (or principal components of the mixture spectra) were extracted using PCA and fed into the MCR analysis as the initial guess of the PCs. PCA analysis also provides the number of PCs and the sample outliers. MCR describes each spectrum, I, as the linear combination of the orthogonal pure component matrix and a profile matrix, s_i.

$$I = \sum \vec{s}_i \cdot \vec{l}_i + \vec{E}, \qquad \text{(Equation 1)}$$

where E stands for the error or variance unexplained by the model used. The profile matrix, s_i, represents the weighting factor of the PCs along the row direction.

SUPPLEMENTAL INFORMATION

Supplemental Information can be found online at https://doi.org/10.1016/j.joule.2019.05.026.

ACKNOWLEDGMENTS

This work is supported by the U.S. Department of Energy's Vehicle Technologies Office under the Silicon Electrolyte Interface Stabilization (SEISta) Consortium directed by Brian Cunningham and managed by Anthony Burrell. We thank Drs. Ilia N. Ivanov, Sergei V Kalinin, and Vera Bocharova for the fruitful discussion. This manuscript has been authored by UT-Battelle, LLC under Contract No. DE-AC05-00OR22725 with the U.S. Department of Energy. The United States Government retains and the publisher, by accepting the article for publication, acknowledges that the United States Government retains a non-exclusive, paid-up, irrevocable, world-wide license to publish or reproduce the published form of this manuscript, or allow others to do so, for United States Government purposes. The Department of Energy will provide public access to these results of federally sponsored research in accordance with the DOE Public Access Plan (http://energy.gov/downloads/doe-public-access-plan).

AUTHOR CONTRIBUTIONS

J.N. conceived the original idea. J.N. and G.Y. organized the project. G.Y. and J.N. drafted the manuscript. D.N.V., A.S., and G.Y. designed and performed the TERS experiments. G.Y. conducted the electrochemical and AFM, SEM measurements on a-Si anodes, and FDTD simulations. G.Y. and X.L. conducted PCA-MCR analysis. T.H. and K.P. conducted the M.D. simulation and DFT calculations. R.E.R., M.N., and G.M.V. assisted with the electrochemical measurements and data analysis a-Si thin film anode preparation. All authors contributed to the editing of the manuscript.

DECLARATION OF INTERESTS

The authors declare no competing interest.

Received: November 23, 2018
Revised: January 7, 2019
Accepted: May 29, 2019
Published: June 20, 2019

REFERENCES

1. Peled, E. (1979). The electrochemical behavior of alkali and alkaline earth metals in nonaqueous battery systems—the solid electrolyte interphase model. J. Electrochem. Soc. *126*, 2047–2051.

2. Pang, Q., Liang, X., Shyamsunder, A., and Nazar, L.F. (2017). An in vivo formed solid electrolyte surface layer enables stable plating of li metal. Joule *1*, 871–886.

3. Yang, C., Chen, J., Qing, T., Fan, X., Sun, W., von Cresce, A., Ding, M.S., Borodin, O., Vatamanu, J., Schroeder, M.A., et al. (2017). 4.0 V aqueous Li-Ion batteries. Joule *1*, 122–132.

4. Son, S.B., Gao, T., Harvey, S.P., Steirer, K.X., Stokes, A., Norman, A., Wang, C., Cresce, A., Xu, K., and Ban, C. (2018). An artificial interphase enables reversible magnesium chemistry in carbonate electrolytes. Nat. Chem. *10*, 532–539.

5. Tu, Z., Choudhury, S., Zachman, M.J., Wei, S., Zhang, K., Kourkoutis, L.F., and Archer, L.A. (2017). Designing artificial solid-electrolyte interphases for single-ion and high-efficiency transport in batteries. Joule *1*, 394–406.

6. Verma, P., Maire, P., and Novák, P. (2010). A review of the features and analyses of the solid electrolyte interphase in Li-Ion batteries. Electrochim. Acta *55*, 6332–6341.

7. Peled, E., and Menkin, S. (2017). Review—SEI: past, present and future. J. Electrochem. Soc. *164*, A1703–A1719.

8. Peled, E., Golodnitsky, D., Ardel, G., Eshkenazy, V., and The, S.E.I. (1995). The sei model—application to lithium-polymer electrolyte batteries. Electrochim. Acta *40*, 2197–2204.

9. Zaban, A., Zinigrad, E., and Aurbach, D. (1996). Impedance spectroscopy of li electrodes. 4. A General Simple model of the li– solution interphase in polar aprotic systems. J. Phys. Chem. *100*, 3089–3101.

10. Peled, E., Tow, D.B., Merson, A., Gladkich, A., Burstein, L., and Golodnitsky, D. (2001). Composition, depth profiles and lateral distribution of materials in the SEI built on Hopg-Tof sims and XPS studies. J. Power Sources *97–98*, 52–57.

11. Zhuang, G.V., Yang, H., Blizanac, B., and Ross, P.N. (2005). A study of electrochemical reduction of ethylene and propylene carbonate electrolytes on graphite using ATR-FTIR spectroscopy. Electrochem. Solid-State Lett. *8*, A441–A445.

12. Ruther, R.E., Hays, K.A., An, S.J., Li, J., Wood, D.L., and Nanda, J. (2018). Chemical evolution in silicon–graphite composite anodes investigated by vibrational spectroscopy. ACS Appl. Mater. Interfaces.

13. Wang, F., Borodin, O., Ding, M.S., Gobet, M., Vatamanu, J., Fan, X., Gao, T., Eidson, N., Liang, Y., Sun, W., et al. (2018). Hybrid aqueous/non-aqueous electrolyte for safe and high-energy Li-Ion batteries. Joule *2*, 927–937.

14. Marino, C., Darwiche, A., Dupré, N., Wilhelm, H.A., Lestriez, B., Martinez, H., Dedryvère, R., Zhang, W., Ghamouss, F., Lemordant, D., et al. (2013). Study of the electrode/electrolyte interface on cycling of a conversion type electrode material in li batteries. J. Phys. Chem. C *117*, 19302–19313.

15. Veith, G.M., Doucet, M., Sacci, R.L., Vacaliuc, B., Baldwin, J.K., and Browning, J.F. (2017). Determination of the solid electrolyte interphase structure grown on a silicon electrode using a fluoroethylene carbonate additive. Sci. Rep. *7*, 6326.

16. Sacci, R.L., Bañuelos, J.L., Veith, G.M., Littrell, K.C., Cheng, Y.Q., Wildgruber, C.U., Jones, L.L., Ramirez-Cuesta, A.J., Rother, G., and Dudney, N.J. (2015). Structure of spontaneously formed solid-electrolyte interphase on lithiated graphite determined using small-angle neutron scattering. J. Phys. Chem. C *119*, 9816–9823.

17. Vogl, U.S., Lux, S.F., Crumlin, E.J., Liu, Z., Terborg, L., Winter, M., and Kostecki, R. (2015). The mechanism of SEI formation on a single crystal si (100) electrode. J. Electrochem. Soc. *162*, A603–A607.

18. Wang, A., Kadam, S., Li, H., Shi, S., and Qi, Y. (2018). Review on modeling of the anode solid electrolyte interphase (SEI) for lithium-ion batteries. NPJ Comp. Mater. *4*, 15.

19. Stöckle, R.M., Suh, Y.D., Deckert, V., and Zenobi, R. (2000). Nanoscale chemical analysis by tip-enhanced Raman spectroscopy. Chem. Phys. Lett. *318*, 131–136.

20. Yang, G., Ivanov, I.N., Ruther, R.E., Sacci, R.L., Subjakova, V., Hallinan, D.T., and Nanda, J. (2018). Electrolyte solvation structure at solid–liquid interface probed by nanogap surface-enhanced Raman spectroscopy. ACS Nano *12*, 10159–10170.

21. Yang, G., Nanda, J., Wang, B., Chen, G., and Hallinan, D.T. (2017). Self-assembly of large gold nanoparticles for surface-enhanced Raman spectroscopy. ACS Appl. Mater. Interfaces *9*, 13457–13470.

22. Yang, G., Sacci, R.L., Ivanov, I.N., Ruther, R.E., Hays, K.A., Zhang, Y., Cao, P.-F., Veith, G.M., Dudney, N.J., Saito, T., et al. (2019). Probing electrolyte solvents at solid/liquid interface using gap-mode surface-enhanced Raman spectroscopy. J. Electrochem. Soc. *166*, A178–A187.

23. Kim, H., Kosuda, K.M., Van Duyne, R.P., and Stair, P.C. (2010). Resonance Raman and surface-and tip-enhanced Raman spectroscopy methods to study solid catalysts and heterogeneous catalytic reactions. Chem. Soc. Rev. *39*, 4820–4844.

24. Zhang, W., Yeo, B.S., Schmid, T., and Zenobi, R. (2007). Single molecule tip-enhanced Raman spectroscopy with silver tips. J. Phys. Chem. C *111*, 1733–1738.

25. Anderson, M.S. (2000). Locally enhanced Raman spectroscopy with an atomic force microscope. Appl. Phys. Lett. *76*, 3130–3132.

26. Hayazawa, N., Inouye, Y., Sekkat, Z., and Kawata, S. (2000). Metallized tip amplification of near-field Raman scattering. Opt. Commun. *183*, 333–336.

27. Deckert-Gaudig, T., Kämmer, E., and Deckert, V. (2012). Tracking of nanoscale structural variations on a single amyloid fibril with tip-enhanced Raman scattering. J. Biophotonics *5*, 215–219.

28. Lapin, Z.J., Beams, R., Cançado, L.G., and Novotny, L. (2015). Near-field Raman spectroscopy of nanocarbon materials. Faraday Discuss *184*, 193–206.

29. El-Khoury, P.Z., Hu, D., Apkarian, V.A., and Hess, W.P. (2013). Raman scattering at plasmonic junctions shorted by conductive molecular bridges. Nano Lett. *13*, 1858–1861.

30. Liao, M., Jiang, S., Hu, C., Zhang, R., Kuang, Y., Zhu, J., Zhang, Y., and Dong, Z. (2016). Tip-enhanced Raman spectroscopic imaging of individual carbon nanotubes with subnanometer resolution. Nano Lett. *16*, 4040–4046.

31. Bailo, E., and Deckert, V. (2008). Tip-enhanced Raman spectroscopy of single rna strands: towards a novel direct-sequencing method. Angew. Chem. Int. Ed. *47*, 1658–1661.

32. Kawata, S., Ichimura, T., Taguchi, A., and Kumamoto, Y. (2017). Nano-Raman scattering microscopy: resolution and enhancement. Chem. Rev. *117*, 4983–5001.

33. Veith, G.M., Doucet, M., Baldwin, J.K., Sacci, R.L., Fears, T.M., Wang, Y., and Browning, J.F. (2015). Direct determination of solid-electrolyte interphase thickness and composition as a function of state of charge on a silicon anode. J. Phys. Chem. C *119*, 20339–20349.

34. Michan, A.L., Leskes, M., and Grey, C.P. (2016). Voltage dependent solid electrolyte interphase formation in silicon electrodes: monitoring the formation of organic decomposition products. Chem. Mater *28*, 385–398.

35. Schroder, K., Alvarado, J., Yersak, T.A., Li, J., Dudney, N., Webb, L.J., Meng, Y.S., and Stevenson, K.J. (2015). The effect of fluoroethylene carbonate as an additive on the solid electrolyte interphase on silicon lithium-ion electrodes. Chem. Mater. *27*, 5531–5542.

36. Jaumann, T., Balach, J., Langklotz, U., Sauchuk, V., Fritsch, M., Michaelis, A., Teltevskij, V., Mikhailova, D., Oswald, S., Klose, M., et al. (2017). Lifetime vs. rate capability: understanding the role of FEC and VC in high-energy Li-Ion batteries with nano-silicon anodes. Energy Storage Mater *6*, 26–35.

37. Yoon, T., Milien, M.S., Parimalam, B.S., and Lucht, B.L. (2017). Thermal decomposition of the solid electrolyte interphase (SEI) on silicon electrodes for lithium ion batteries. Chem. Mater. *29*, 3237–3245.

38. Zhuang, G.V., Xu, K., Yang, H., Jow, T.R., and Ross, P.N. (2005). Lithium ethylene dicarbonate identified as the primary product of chemical and electrochemical reduction of EC in 1.2 M $LiPF_6$/EC: EMC electrolyte. J. Phys. Chem. B *109*, 17567–17573.

39. Socrates, G. (2001). Infrared and Raman characteristic group frequencies: tables and charts (John Wiley & Sons).

40. Nie, M., Abraham, D.P., Chen, Y., Bose, A., and Lucht, B.L. (2013). Silicon solid electrolyte interphase (SEI) of lithium ion battery characterized by microscopy and spectroscopy. J. Phys. Chem. C *117*, 13403–13412.

41. Banik, M., El-Khoury, P.Z., Nag, A., Rodriguez-Perez, A., Guarrottxena, N., Bazan, G.C., and Apkarian, V.A. (2012). Surface-enhanced Raman trajectories on a nano-dumbbell: transition from field to charge transfer plasmons as the spheres fuse. ACS Nano *6*, 10343–10354.

42. Agapov, R.L., Malkovskiy, A.V., Sokolov, A.P., and Foster, M.D. (2011). Prolonged blinking with TRES probes. J. Phys. Chem. C *115*, 8900–8905.

43. Brooker, M.H., and Bates, J.B. (1971). Raman and infrared spectral studies of anhydrous Li_2CO_3 and Na_2CO_3. J. Chem. Phys. *54*, 4788–4796.

44. Schroder, K.W., Celio, H., Webb, L.J., and Stevenson, K.J. (2012). Examining solid electrolyte interphase formation on crystalline silicon electrodes: Influence of electrochemical preparation and ambient exposure conditions. J. Phys. Chem. C *116*, 19737–19747.

45. An, S.J., Li, J., Sheng, Y., Daniel, C., and Wood, D.L. (2016). Long-term lithium-ion battery performance improvement via ultraviolet light treatment of the graphite anode. J. Electrochem. Soc. *163*, A2866–A2875.

46. Shi, F., Ross, P.N., Somorjai, G.A., and Komvopoulos, K. (2017). The chemistry of electrolyte reduction on silicon electrodes revealed by in situ ATR-FTIR spectroscopy. J. Phys. Chem. C *121*, 14476–14483.

47. Giorgini, M.G., Futamatagawa, K., Torii, H., Musso, M., and Cerini, S. (2015). Solvation structure around the Li+ ion in mixed cyclic/linear carbonate solutions unveiled by the Raman noncoincidence effect. J. Phys. Chem. Lett. *6*, 3296–3302.

48. Moskovits, M. (1982). Surface selection rules. J. Chem. Phys. *77*, 4408–4416.

49. Gallego, N.C., Contescu, C.I., Meyer, H.M., III, Howe, J.Y., Meisner, R.A., Payzant, E.A., Lance, M.J., Yoon, S.Y., Denlinger, M., and Wood, D.L., III (2014). Advanced surface and microstructural characterization of natural graphite anodes for lithium ion batteries. Carbon *72*, 393–401.

50. Kurouski, D., Mattei, M., and Van Duyne, R.P. (2015). Probing redox reactions at the nanoscale with electrochemical tip-enhanced Raman spectroscopy. Nano Lett. *15*, 7956–7962.

51. Kang, G., Yang, M., Mattei, M.S., Schatz, G.C., and Van Duyne, R.P. (2019). *In-situ* nanoscale redox mapping using tip-enhanced Raman spectroscopy. Nano Lett.

52. Zeng, Z.C., Huang, S.C., Wu, D.Y., Meng, L.Y., Li, M.H., Huang, T.X., Zhong, J.H., Wang, X., Yang, Z.L., and Ren, B. (2015). Electrochemical

tip-enhanced Raman spectroscopy. J. Am. Chem. Soc. *137*, 11928–11931.

53. Wang, X., Huang, S.C., Huang, T.X., Su, H.S., Zhong, J.H., Zeng, Z.C., Li, M.H., and Ren, B. (2017). Tip-enhanced Raman spectroscopy for surfaces and interfaces. Chem. Soc. Rev. *46*, 4020–4041.

54. Borodin, O., Suo, L., Gobet, M., Ren, X., Wang, F., Faraone, A., Peng, J., Olguin, M., Schroeder, M., Ding, M.S., et al. (2017). Liquid structure with nano-heterogeneity promotes cationic transport in concentrated electrolytes. ACS Nano *11*, 10462–10471.

55. Hartschuh, A. (2008). Tip-enhanced Near-Field Optical Microscopy. Angew. Chem. Int. Ed. *47*, 8178–8191.

56. Agapov, R.L., Sokolov, A.P., and Foster, M.D. (2013). Protecting TERS probes from degradation: extending mechanical and chemical stability. J. Raman Spectrosc. *44*, 710–716.

57. Barrios, C.A., Malkovskiy, A.V., Kisliuk, A.M., Sokolov, A.P., and Foster, M.D. (2009). Highly stable, protected plasmonic nanostructures for tip-enhanced Raman spectroscopy. J. Phys. Chem. C *113*, 8158–8161.

58. Johnson, P.B., and Christy, R.W. (1972). Optical constants of the noble metals. Phys. Rev. B *6*, 4370–4379.

59. Frisch, M.J., Trucks, G.W., Schlegel, H.B., Scuseria, G.E., Robb, M.A., Cheeseman, J.R., Scalmani, G., Barone, V., Petersson, G.A., Nakatsuji, H., et al. (2016) Gaussian 16 Rev. A.03.

60. Becke, A.D. (1993). Density-functional thermochemistry. Iii. The role of exact exchange. J. Chem. Phys. *98*, 5648–5652.

61. Martens, H., and Naes, T. (1989). Multivariate calibration (John Wiley & Sons).